Quantitative Evaluation of Metal Artifact Reduction in CBCT: Effects of Exposure Dose and Metal Direction

Chul Wan Park

The Graduate School
Yonsei University
Department of Industrial Dentistry

Quantitative Evaluation of Metal Artifact Reduction in CBCT: Effects of Exposure Dose and Metal Direction

A Master's Thesis Submitted
to the Department of Industrial Dentistry
and the Graduate School of Yonsei University
in partial fulfillment of the
requirements for the degree of
Master in Applied Life Science

Chul Wan Park

February 2025

This certifies that the Master's Thesis of Chul Wan Park is approved

Thesis Supervisor Sang-Sun Han

Thesis Committee Member Kug Jin Jeon

Thesis Committee Member Chena Lee

The Graduate School
Yonsei University
February 2025

감사의 글

내 인생에서 가장 큰 도전 중 하나였으며, 다사다난했던 나날들을 지나 드디어 마무리를 하게 되었습니다. 많은 분들의 아낌없는 격려와 도움이 있어서 여기까지 올 수 있었습니다. 이 논문이 완성될 수 있도록 도와주신 분들께 감사의 말씀을 전합니다.

도전에 가까웠던 석사 과정을 잘 마무리 할 수 있도록 지원을 아끼지 않으셨던 지도교수이신 한상선 교수님께 깊은 감사의 말씀 올립니다. 어떻게 시작해야 하는지도 몰라서 전전긍긍할 때부터 길라잡이가 되어 주셨고, 항상 용기를 북돋아 주시고, 격려해 주셔서 자신감을 잃지 않고 끝까지 완주 할 수 있었습니다. 바쁘신 일정에도 먼저 손을 내밀어주시고, 만나 뵐 때마다 따뜻한 말씀과 조언을 해주셨습니다. 선배님을 찾아 뵙는다는 생각을 가질 만큼 편하게 대해주셔서 너무 감사했습니다. 연구 대한 방향뿐만 아니라 꼼꼼하지 못해 실수투성이인 저에게 논문 작성방법 같은 세부적인 사항까지 친절하게 지도해주셔서 감사했습니다. 교수님께서 보여주신 애정과 격려 덕분에 모든 과정을 무사히 마쳐 자랑스러운 결과물을 만들 수 있었습니다. 이번에 배운 지식과 경험들을 바탕으로 더욱 성장할 수 있는 사람이 되겠습니다.

또한, 연구에 대한 고민과 조언을 아끼지 않으신 전국진 교수님, 이채나 교수님 감사합니다. 다양한 연구 방법과 해석에 대해 새로운 생각과 고민하는 방법을 배울 수 있어서 한층 성장할 수 있는 계기가 되었습니다. 귀중한 조언을 해주셔서 감사 드립니다. 실험 설계부터 완성도를 높일 수 있도록 다양한 토론과 직접적인 지원을 아끼지 않으신 조규동 교수님께도 감사의 말씀을 드리고 싶습니다. 격려해 주신 최윤주 교수님께도 감사 드리고, 항상 친절하게 대해주신 영상치의학과 선생님들께도 감사의 말씀 전합니다.

2년이라는 시간 동안 동기들과 서로 의지하고 서로의 버팀목이 되어주어 힘이 되었습니다. 고생하고 노력한 만큼 다 함께 좋은 결과를 얻게 되어 너무나 자랑스럽고, 부끄럽지만 고마운 마음을 전하고 싶습니다.

부족한 제게 연세대학교 석사라는 꿈을 이룰 수 있는 기회를 주신 유재호 본부장님께 감사 드립니다. 일과 학업을 병행 할 수 있도록 배려해주시고 지원해 주신 이금용 실장님과 최종원 실장님께도 감사의 말씀 드립니다. 연구 실험을 진행할 수 있도록 적극적인 지원을 해주신 조민국 연구소장님께 감사 드리고, 정현섭 실장님, 이현우 연구원에게도 감사합니다. 많은 일들로 힘들어하던 제게 안팎으로 응원해 준 마케팅본부 선후배 동료들에게도 감사하다는 말을 전하고 싶습니다.

마지막으로 사랑하는 나의 가족들에게 고마운 마음을 전합니다. 전적으로 믿어주고 응원해 주었던 평생의 동반자인 아내 백송이, 존경하고 사랑합니다. 내 인생의 가장 큰 보물인 별하, 재하야 건강하게 자라줘서 고맙고 사랑해. 말없이 뒤를 바쳐주시는 아빠, 항상 최고라고 말씀해주시는 엄마 감사하고 사랑합니다. 항상 건강하세요. 나의 절친이자 쉼터인 우리 형한테도 항상 고맙고 사랑한다고 전하고 싶습니다.

많은 분들의 배려와 응원 덕분에 열매를 맺을 수 있었습니다. 감사 드리고 싶은 모든 분들을 하나하나 언급하지 못해 죄송합니다. 이러한 과분한 사랑을 나눌 수 있는 큰 사람이 되기 위해 노력하겠습니다. 감사합니다.

TABLE OF CONTENTS

LIST OF FIGURES

LIST OF TABLES

ABSTRACT

Quantitative Evaluation of Metal Artifact Reduction in CBCT : Effects of Exposure Dose and Metal Direction

Purpose:

Various metal artifact reduction (MAR) methods for cone-beam computed tomography (CBCT) have been recently introduced, but there is a lack of information on how to quantitatively evaluate their effectiveness. This study aims to establish a standardized experimental method utilizing a quality-assured CBCT phantom, and to evaluate the MAR effectiveness by measuring the area of metal artifacts compared to MAR on/off for scanned CBCT images.

Methods:

A sedentex-CT phantom with multiple titanium metal rods inserted in both horizontal and vertical direction was scanned using a CBCT device. CBCT scans were repeated in three exposure protocol (standard dose, low dose, ultra-low dose) with the MAR function on and off. The area of metal artifacts on all acquired images was measured using ImageJ software to evaluate the effect of MAR. The differences in artifact area values between MAR on and off were statistically analyzed according to each exposure protocols and metal direction.

Results:

Artifact areas on CBCT images with the MAR function were significantly reduced compared to those without MAR across all exposure protocols and metal direction (P

< 0.05). The artifact areas showed the greatest reduction in the ultra-low dose protocol (80.3%, from 262.30 mm^2 to 51.72 mm^2), followed by the low dose protocol (73.6%, from 331.59 mm^2 to 87.66 mm^2) and the standard dose protocol (61.5%, from 358.28 mm^2 to 137.83 mm^2). The reduction rate was higher for the vertical metal direction (80.7%, from 276.96 mm^2 to 53.36 mm^2) than the horizontal direction (63.3%, from 357.82 mm^2 to 131.45 mm^2).

Conclusion:

This study quantitatively demonstrates the performance of the MAR in consistently reducing metal artifacts in various radiation dose protocols and metal directions. In particular, the effect of percentage reduction was excellent when the exposure protocol with low radiation dose and the metal condition were vertical in the scanned CBCT. This established method, involving quantitative measurement of artifact areas, provides a valuable framework for future research in artifact reduction and potential optimization in clinical applications.

Key words : cone beam computed tomography; metal artifact reduction; CBCT phantom; exposure protocol; metal directions; percentage reduction

1. INTRODUCTION

Since the introduction of cone beam computed tomography (CBCT) devices into clinical practice in the early 1990s, they have been increasingly used in diagnostic and treatment planning in the dental field. The reason is that the technological advancement of the key components for image implementation has improved the image quality, with less radiation exposure and smaller equipment footprint compared to the multi detector computed tomography (MDCT). CBCT is a tomography device that positions the target object between a cone-beam x-ray generator and a flat-panel detector, obtaining image data by rotating the gantry once around the object and reconstructing uniform cross-sectional images. Compared to MDCT, which requires multiple rotations, CBCT achieves diagnostic imaging with relatively lower radiation exposure. However, due to the use of a dimensional flat-panel detector instead of the fan-beam x-ray and linear detector array in MDCT, CBCT generates 4-5 times more scattered radiation, resulting in lower signal-to-noise ratio and reduces contrast resolution (Zhang et al., 2007; Jacobs et al., 2018; Lim, Jung, & Lee, 2005; Korpics et al., 2016; Queiroz et al., 2017; Choi, Kim, & Hwang, 2006).

In particular, when scanning metal materials using CBCT, such as stainless steel used to make prosthetics or titanium materials used to process implants, beam hardening and scattering occur. These artificial transformation are called metal artifact. (Queiroz et al., 2017; Choi, Kim, & Hwang, 2006) These metal artifacts can degrade the quality of images and act as a hindrance to the diagnosis of anatomical structures, thus reducing the accuracy of diagnosis and treatment plans. (Choi, Kim, & Hwang, 2006; Park, Jeon, & Seo, 2023). The main types of artifact occurring are streak artifact and beam hardening artifact. Beam hardening artifacts occur between low-permeability materials, such as metals, when lower-energy rays are absorbed and higher-energy rays pass through, causing energy shifts. This often causes certain areas around the metal to appear dark or shaded (Barrett & Keat, 2004; Washio et al., 2020). Streak artifacts appear as light streaks or dark streaks in the image and are typically

caused by photon starvation or x-ray scattering around high-density objects (Korpics et al., 2016; Washio et al., 2020).

These artifacts can be mitigated by increasing the tube current and voltage to increase the number of photons, or generating high-energy photons to penetrate denser materials, thereby reduce noise and photon deficiency in the image. However, it is not generally suitable for application because it relatively affects the reduction of tissue contrast and increases the amount of radiation exposed to patients (Choi, Kim, & Hwang, 2006; Kunz et al., 2022).

Therefore, Metal artifact reduction (MAR) techniques are widely used to minimize artifacts caused by metals for decreasing radiation exposure. Since its introduction in the 1980s, MAR has employed various approaches and continues to be developed and improved (Queiroz et al., 2017; Nazir & Mushtaq, 2024; Kalender, Hebel, & Ebersberger, 1987). Representative methods include iterative reconstruction techniques like expectation maximization and algebraic reconstruction technique, which correct incomplete data, as well as projection-based method that interpolates or estimates missing or distorted data (Yu et al., 2009; Boudabbous et al., 2015). Recently, artificial intelligence-driven deep learning MAR technology, which detects and optimizes artifacts automatically has become commercially available and is offered by many CBCT manufacturers (Yu et al., 2009; Boudabbous et al., 2015; Wang, Vannier, & Cheng, 1999; Ghani & Karl, 2020; Lee, Kim, & Cho, 2024).

Various CBCT equipment offering MAR function have been introduced, there is a lack of information focused on standardized methods of effectiveness evaluation about MAR. Only some previous researchers used phantoms arbitrarily created or regions of interest (ROI) subjectively selected for metal artifact evaluation (Zhang et al., 2007; Jacobs et al., 2018; Lim, Jung, & Lee, 2005; Korpics et al., 2016; Queiroz et al., 2017). There are few studies analyzing the reduction effectiveness of metal artifact in CBCT. Thus the objective and standardized methods for metal artifact reduction evaluations in need.

This research aimed to establish a standardized method by quantitatively analyzing the measurement of MAR area on CBCT images using quality assurance (QA) phantom across three CBCT exposure protocols (standard, low dose, ultra-low dose) and different orientations of consecutive metal direction. We also perform effectiveness evaluation on scanned CBCT equipment.

2. MATERIALS AND METHODS

2.1. Acquiring CBCT images

All images were acquired using the T2 PLUS CBCT (T2 PLUS-CS, OSSTEM IMPLANT Co., Ltd., Siheung, South Korea). This system is a dental CBCT, consisting of an x-ray tube and an IGZO-type flat panel detector. It also includes a metal artifact reduction function based on deep learning-based metal extraction.

In CBCT, parameters such as the field of view (15 × 9 cm), tube voltage (95 kV), and voxel size (200 μm^2) were kept constant across all scans, while tube current, exposure time, and binning mode were adjusted according to the specific exposure protocols.

CBCT was taken under various conditions to compare the difference in effectiveness of MAR. By default, we set up the exposure protocols: standard, low dose, and ultra-low dose considering the difference in radiation exposure. We used the exposure protocol provided by the manufacturer, and the tube current and exposure time were changed, and conditions such as imaging field of view, tube voltage, angle, and rotation radius were fixed as shown in the following Table 1.

Table 1. CBCT exposure protocols

Exposure protocols	MAR	FOV (cm^2)	Voxel size (μm^2)	Tube voltage (kV)	Tube current (mA)	Exposure time (s)	DAP ($\mu Gy \times m^2$)
Standard	Off	15 x 9	200	95	6	22	238.7
	On						
Low dose	Off	15 x 9	200	95	6	10	111.4
	On						
Ultra-low dose	Off	15 x 9	200	95	3	10	53.3
	On						

MAR; metal artifact reduction, FOV; field of view, DAP; dose area product

Images were reconstructed with raw data obtained by the protocol to obtain MAR on and MAR off images, respectively. The acquired images were stored in the form of digital imaging and communication (DICOM).

2.2. Acquiring QA phantom imaging

To increase the reliability of evaluating MAR effects, scans were performed using CBCT QA phantom of a sedentex-CT (Leeds Test Objects Ltd, North Yorkshire, United Kingdom) with quantitative measurements. The phantom is about the head size and is made of cylindrical polymethyl methacrylate (PMMA). Cylindrical phantom of size of 16×16 cm. The phantoms are designed for use in image quality control of CBCT. The lower portion of the phantom (height: 22 mm) is composed of uniform PMMA. The top section features seven inserts holes (diameter: 35 mm, height: 140 mm) positioned in arranged in a regular hexagonal pattern and around the center. (Figure 1) A total of nine image quality parameters can be tested, including 42 inserts of 13 types (diameter: 35mm, height: 20mm) and the bottom PMMA portion in Table 2.

In this study, we used beam hardening artifacts among the various inserts of the sedentex-CT phantom. Inside the insert, three cylindrical titanium bars of diameter of 5 mm are arranged parallel to each other at 5 mm intervals. The metal bars are 17 mm long and the insert are wrapped in PMMA. The arrangement and position of the inserts followed the method suggested by the manufacturer.

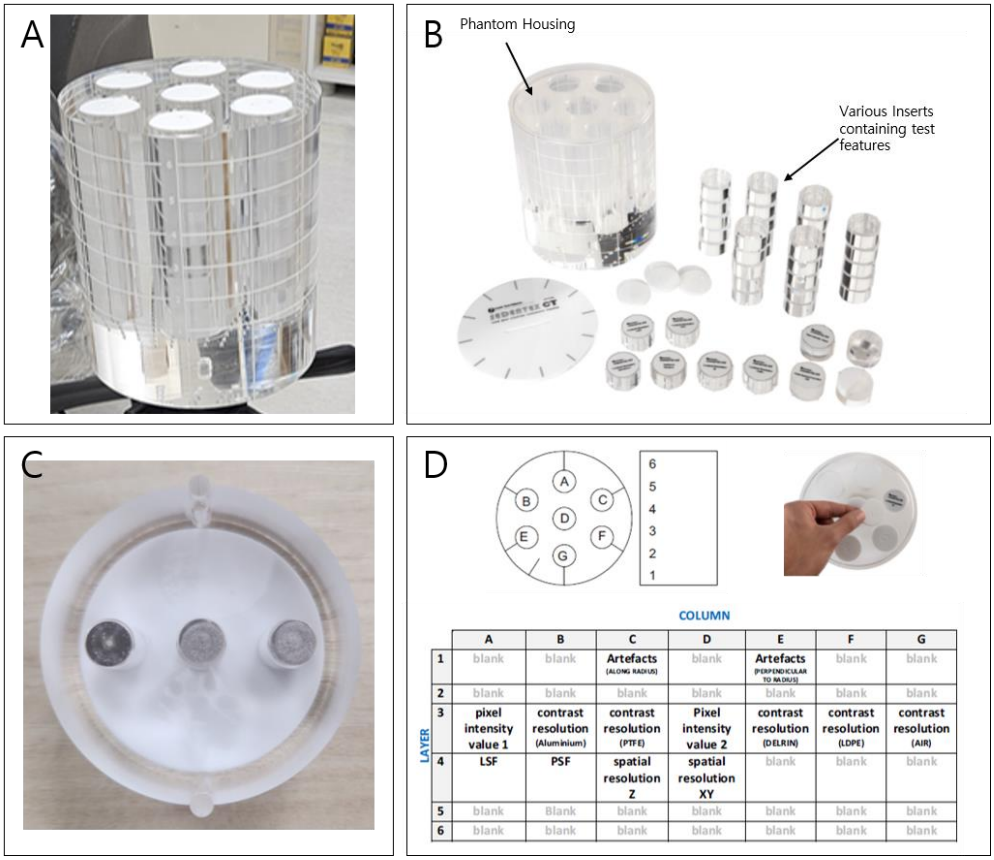

	A	B	C	D	E	F	G
1	blank	blank	Artefacts (ALONG RADIUS)	blank	Artefacts (PERPENDICULAR TO RADIUS)	blank	blank
2	blank	blank	blank	blank	blank	blank	blank
3	pixel intensity value 1	contrast resolution (Aluminium)	contrast resolution (PTFE)	Pixel intensity value 2	contrast resolution (DELRIN)	contrast resolution (LDPE)	contrast resolution (AIR)
4	LSF	PSF	spatial resolution Z	spatial resolution XY	blank	blank	blank
5	blank	Blank	blank	blank	blank	blank	blank
6	blank	blank	blank	blank	blank	blank	blank

Figure 1. Standard protocol for insert location of sedentex-CT phantom

(A) Components of sedentex-CT image quality phantom (B) The sedentex-CT phantom used for evaluating metal artifacts in CBCT (C) Placement of inserts (D) The 'beam hardening artifact' inserts consisting of three cylindrical metals

Table 2. List of the parameters for image analysis and inserts

Mode	Field of view (cm^2)	Layer
Noise/Uniformity	The lower section of the phantom is uniform PMMA (density 1.20 +/- 1.00%)	5/6
Geometric Distortion	An array of 2.0 mm diameter, 3.0 mm deep Air / gaps are uniformly pitched at 10.0 mm intervals through one slice of the cylinder	
Spatial Resolution (LSF)	PMMA/PTFE interface	4
Spatial Resolution (PSF)	stainless steel wire suspended in air	4
LP/mm	alternating Aluminum/polymer (XY)	3
LP/mm	alternating Aluminum/polymer (Z)	3
Contrast Resolution	1.0, 2.0, 3.0, 4.0, 5.0 mm diameter Aluminum, PTFE, delrin, LDPE, Air, Water (PMMA) rods suspended in PMMA	4
Pixel intensity	10.0 mm diameter Aluminum, PTFE, delrin, LDPE, Air, Water (PMMA) rods suspended in PMMA	3
Beam Hardening Artefacts	A line of three 5.0 mm diameter rods of Ti suspended in PMMA	1
Blank PMMA insert		2

PMMA; methyl methacrylate, PTFE; Polytetrafluoroethylene, LDPE; Low Density Polyethylene

The two beam hardening artifacts insert were placed so that successive cylindrical metal objects could face in different directions. The inserts were placed at the same height but left/right edge respectively. The position of the ‘beam hardening artifact’ inserts was taken to be seen in the middle based on height, taking into account the max FOV (15×9) of the imaging equipment.

For all scans, the phantom was taken without moving from the same position. For each exposure protocols (standard, low dose, ultra-low dose), 8 scans were taken. The resulting dataset consisted of a total of 450 axial slice of CBCT, 5 slices were selected from the metal artifact area and 1 slice was selected from the PMMA area for reference.

The cylindrical metal is located between 213 to 298 slices among axial slices. (Slice interval: 0.2 mm, cylindrical metal acquisition area: 85 slices in total) (Figure 2)

To select a representative slice, we identified the center slice of the artifact layer and used this to select two additional slices at equal intervals up and down. PMMA slices were selected for the criteria of the analysis. Six slices (5 analytical slices and 1 reference slice) selected from each scan were stored separately for further image analysis.

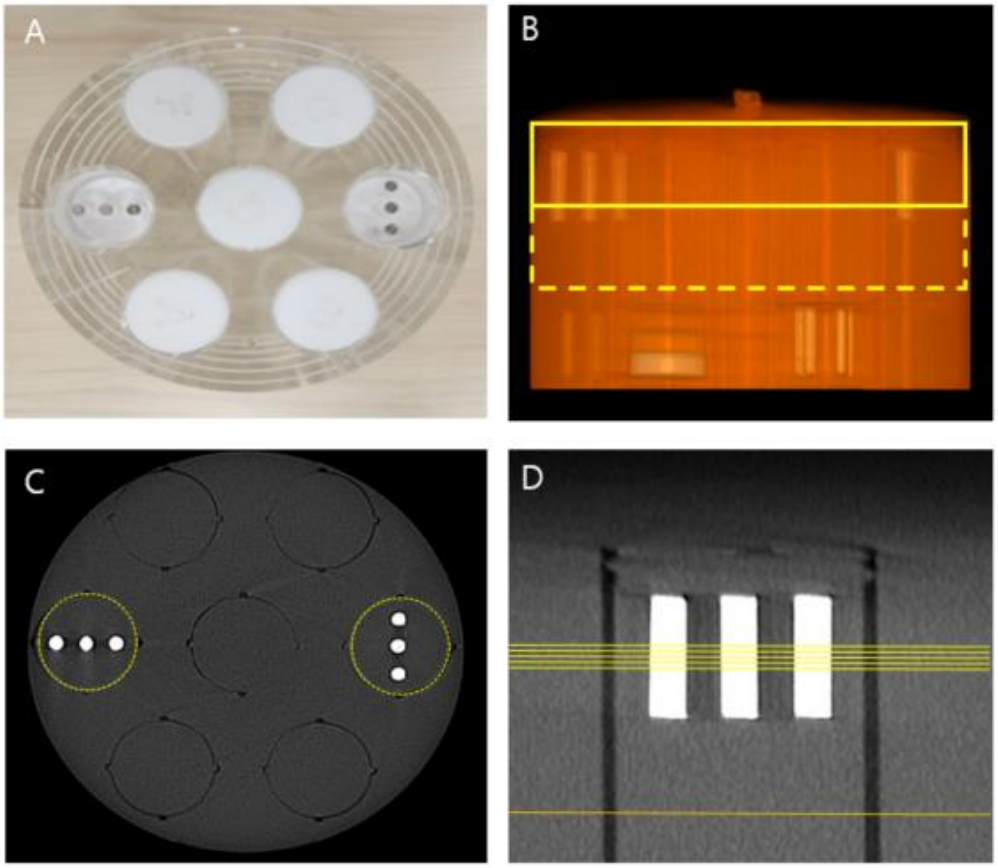

Figure 2. Image acquisition using sedentex-CT phantom

(A) sedentex-CT phantoms_insert insertion direction (B) CBCT projection of phantom, Yellow Box: metal artifact layer, Yellow Dotted Box: PMMA layer (C) Axial slice image with region of interest (Yellow dotted circle) (D) Coronal slice image with region of interest, Yellow Line: analytical slices, Orange Line: reference slice

2.3. Image analysis of artifact area

Considering the size of insert, the ROI was set in a 32mm diameter circle, and the measurement position was defined to be located in the center of the insert to be analyzed.

The mean gray value and standard deviation were calculated by placing ROI in the center of the reference slice consisting of uniform PMMA. This value is set to the reference threshold and the value obtained by adding three times the standard deviation to the corresponding value is set to the maximum threshold and the value obtained by subtracting three times the standard deviation is set to the minimum threshold. The set maximum/minimum threshold was applied as a binary value of five analytical slices. The pixel values between the maximum and minimum threshold values were obtained by placing the ROI in the center of 'beam hardening artifacts' inserts in the analytical slice. The metal artifact areas were represented in black and the PMMA areas unaffected by the metal artifact were represented in white. (Figure 3)

The area of white PMMA area without metal artifacts was excluded from the total area set as the ROI. In addition, the area of metal artifact was calculated excluding the cylindrical metal area and quantified using the following formula.

Metal artifact area = 804.32mm²* – (804.32mm² x white area %) – 58.9mm²**

*804.32 mm² = 32 mm diameter represents the total area of the circular ROI and **58.9 mm² represents the area of the cylindrical metal bar.

ImageJ software (version 1.54g; NIH, Bethesda, MD, USA) was used for data acquisition.

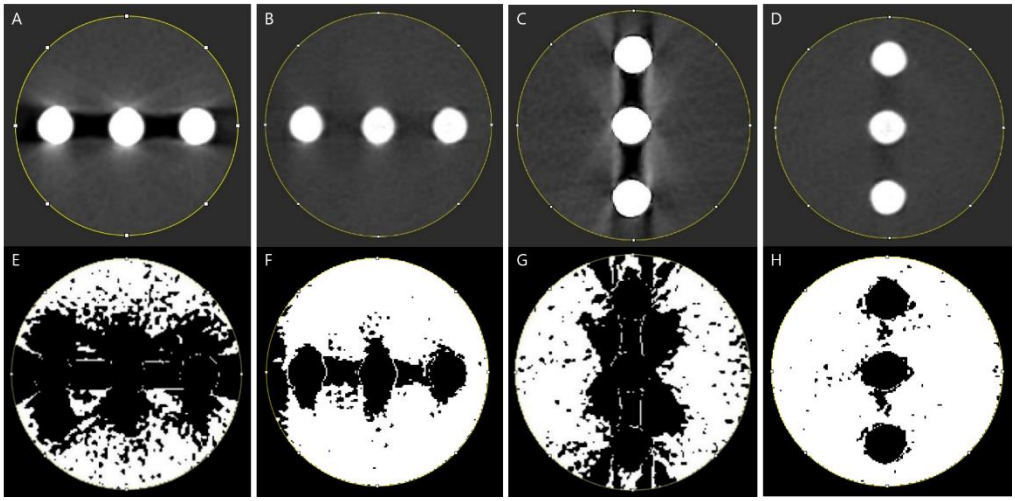

Figure 3. Quantitative image analysis (A, B, C, D): Axial analysis slices showing circular ROI. (E, F, G, H): Axial analysis slices binary using a threshold, where black areas represent the cylindrical metal bars and associated artifacts while white areas correspond to the PMMA regions unaffected by the artifacts. (A, E): MAR off, low-dose exposure protocol, horizontal metal arrangement. (B, F): MAR on, low-dose exposure protocol, horizontal metal arrangement. (C, G): MAR off, low-dose exposure protocol, vertical metal arrangement. (D, H): MAR on, low-dose exposure protocol, vertical metal arrangement.

ROI; region of interest, MAR; metal artifact reduction

The reference axial slices of the CBCT data were imported into ImageJ software to generate images, and the ROI was defined as a 32 mm diameter circle in the center of the image using the 'Specify' function. (Figure 4) The ‘Clear Outside’ function was applied to remove all areas outside the ROI, then the ‘Measure’ function was used to obtain the average gray scale, standard deviation values and record the collected data for analysis.

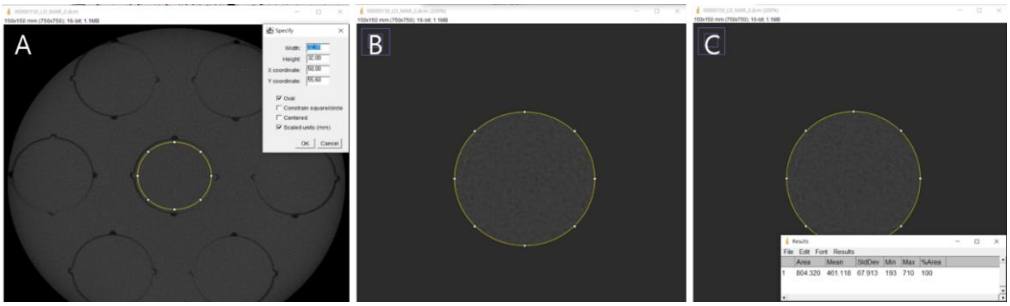

Figure 4. Method of obtaining mean gray scale and standard deviation from reference slices (A) Setting the ROI (B) Erasing images other than the ROI (C) Data acquisition

Analysis of CBCT data axial slices were imported into ImageJ software to create an image and the 'Specify' function was used to define a ROI with a diameter of 32 mm in the center of the vertical metal rods. The ‘Clear Outside’ function was applied to remove all areas outside the ROI. The image was binarized by entering the minimum and maximum threshold values in the ‘Threshold’ function. The percentage area (PMMA area unaffected by artifacts) was measured using the ‘Measure’ function, and the obtained data was recorded. (Figure 5)

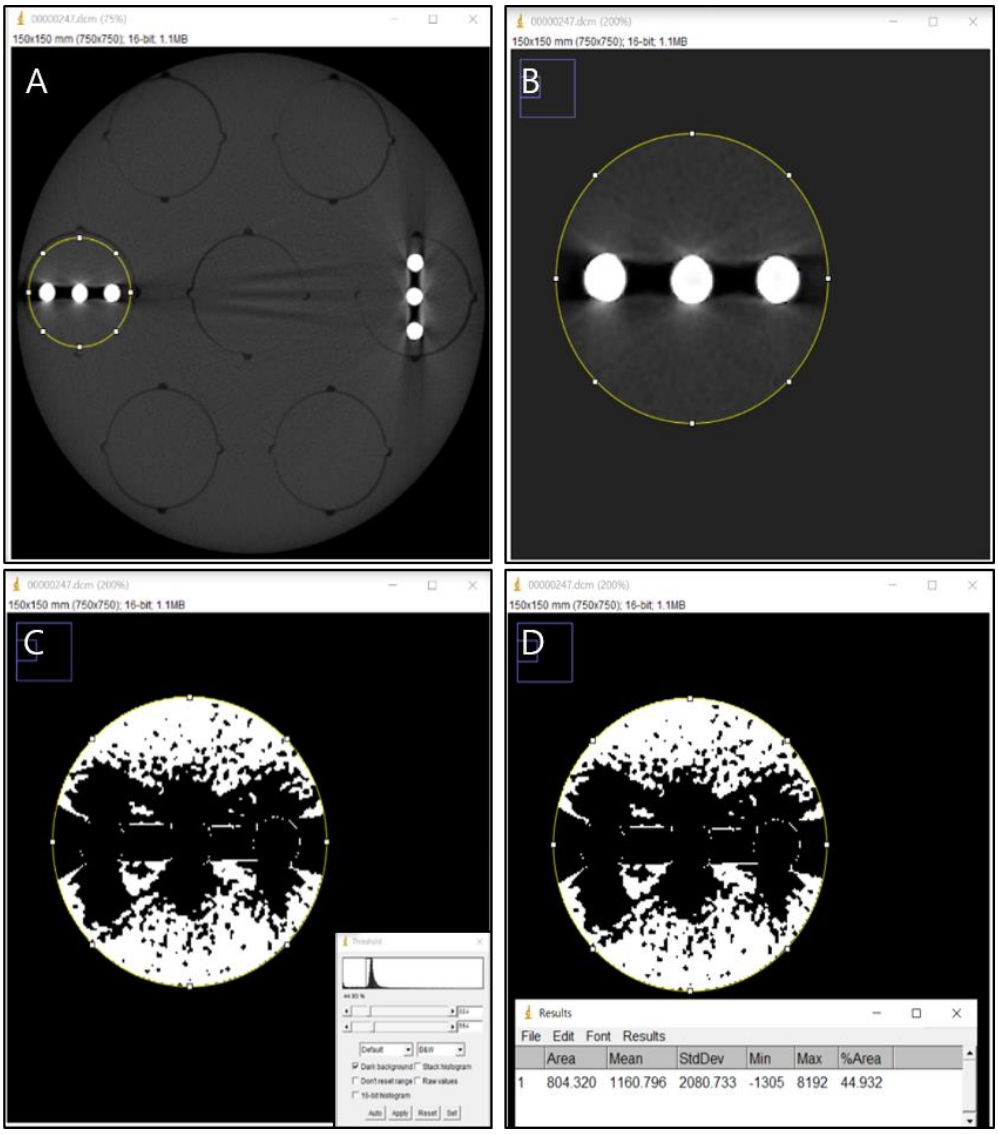

Figure 5. Calculation of the white percentage area of the analytical slice (A) Set the size and position of the ROI (B) Delete the region other than the ROI (C) Apply the threshold to obtain binary slice image (D) Acquire data

2.4 Statistical analysis

The above experimental method calculated and analyzed the area value of the artifact with a total of 480 slice data, 40 samples for each condition (Table 3). Statistical analysis was performed using SPSS software (version 25.0; IBM Corp., Armonk, NY, USA). Due to the non-parametric nature of the data, a Wilcoxon signed-rank test was used to compare the artifact areas before and after the application of the MAR algorithm across different exposure protocols and rod direction. A significance level of $p < 0.05$ was considered statistically significant. The effect size was calculated using ‘Cohen's d’ to assess the magnitude of artifact reduction, interpreted based on standard guidelines (small: 0.2, medium: 0.5, large: 0.8). In order to objectively compare the differences in the effects of MAR measured differently for each imaging protocol, the percentage reduction value was defined and calculated using the following equation.

Percentage reduction: (artifact area of MAR off − artifact area of MAR on) / artifact area of MAR off × 100

Table 3. Selection of axial slice for metal artifact area calculation

	Exposure protocol	Number of scan (n)	Metal direction	Slice (n)	Sample (n)	Total (n)
MAR on	standard	8	vertical	5	40	240
			horizontal	5	40	
	low dose	8	vertical	5	40	
			horizontal	5	40	
	ultra-low dose	8	vertical	5	40	
			horizontal	5	40	
MAR off	standard	8	vertical	5	40	240
			horizontal	5	40	
	low dose	8	vertical	5	40	
			horizontal	5	40	
	ultra-low dose	8	vertical	5	40	
			horizontal	5	40	

3. RESULTS

In this study, a total of 480 regions of interest were analyzed from 240 analytical slices. For image acquisition, a total of 24 raw CT data were acquired 8 times for each of the various exposure protocols (standard, low dose, ultra-low dose), then 48 images were acquired by reconstructing them into images without the MAR algorithm (MAR off) and images with the MAR algorithm (MAR on). Five analysis slices were selected from each image, and 120 slices without the MAR algorithm (MAR off) and 120 slices with the MAR algorithm (MAR on) were analyzed. For the ROI, data were obtained by specifying each slice with metal arranged vertical/horizontal. The evaluation process included various exposure protocols (standard, low dose, ultra-low dose) and direction of three consecutive cylindrical metals (horizontal and vertical).

3.1. Overall effect of the MAR

To compare the data, the mean of the parameters for MAR off (480 samples) and MAR on (480 samples) was calculated to obtain the data. (Table 4) The average artifact area of 120 slices without the MAR algorithm was 317.39mm² (SD: 60.60mm²), and after the MAR algorithm was applied, it was confirmed as 224.99mm² (SD: 31.50mm²). The data were tested by the Wilcoxon signed-rank test and showed a statistically significant difference in the mean between the two groups. (p <0.05)

Table 4. Measured artifact area, differences, and percentage reduction in overall

	MAR Off (mm²)	**MAR on (mm²)**	**Difference (mm²)**	**Percentage Reduction**	***p*-value**
Overall	317.39 ± 60.60	92.40 ± 55.27	224.99 ± 31.50	70.9	<0.05 [a]

[a] Wilcoxon signed-rank test for comparison between MAR off and MAR on. p-value < 0.05 is considered as statistically significant.

3.2. Effect of the MAR according to radiation dose

In all three exposure protocols, a significant reduction effect was confirmed, comparing the artifact area before and after the MAR algorithm. The average artifact area before application of the MAR algorithm was 358.28 mm^2 (SD: 40.28 mm^2) in the standard exposure protocol; after application, it was reduced to 137.83 mm^2 (SD: 57.16 mm^2); after application, it was reduced from 331.59 mm^2 (SD: 50.78 mm^2) to 87.66 mm^2 (SD: 41.45 mm^2) in the low dose exposure protocol; and after the ultra-low dose exposure protocol, the artifact area was reduced from 262.30 mm^2 (SD: 44.01 mm^2) to 51.72 mm^2 (SD: 21.61 mm^2). Therefore, the decrease in percentage was confirmed as 61.5% at standard dose, 73.6% at low dose, and 80.3% at ultra-low dose mode, confirming a significant artifact reduction effect. (p <0.05) The data were validated by the Kruskal Wallace test for comparison. Data between each exposure protocol were tested by Mann-Whitney U test for comparison, and all the resulting values were statistically significant, with p-values <0.05 between the standard and the low dose, between the low dose and the ultra-low dose, and p-values <0.05, between the standard and ultra-low dose. (Figure 6) To compare the data, the percentage reduction of parameters was calculated for standard dose (160 samples: MAR off 80, MAR on 80), low dose (160 samples: MAR off 80, MAR on 80), and ultra-low dose (160 samples: MAR off 80, MAR on 80) to obtain the data. (Table 5)

Table 5. Measured artifact area, differences, and percentage reduction across exposure protocol

Exposure protocol	MAR Off (mm^2)	MAR on (mm^2)	Difference (mm^2)	Percentage reduction	*p*-value [a]
Standard	358.28 ± 40.28	137.83 ± 57.16	220.46 ± 36.35	61.5	<0.05
Low dose	331.59 ± 50.78	87.66 ± 41.45	243.93 ± 22.14	73.6	<0.05
Ultra-low dose	262.30 ± 44.01	51.72 ± 21.61	210.57 ± 24.42	80.3	<0.05

[a] Wilcoxon signed-rank test for compare MAR On and MAR off in the Groups. *p*-value <0.05 is considered as statistically significant.

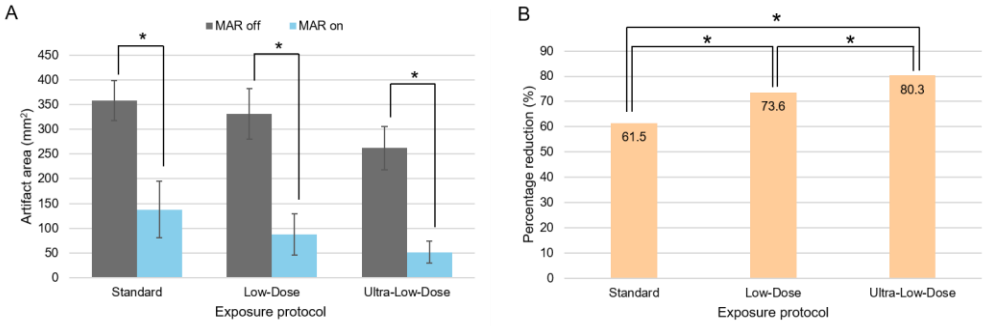

Figure 6. Comparison of metal artifact reduction according to exposure protocol (A) Measured artifact areas (mm^2) across exposure protocol with the MAR algorithm activated and deactivated. Error bars represent standard deviations (* p <0.05, Wilcoxon signed-rank test). (B) Percentage reduction in artifact areas across exposure protocol with the MAR algorithm activated. (* p <0.05, Kruskal-Wallis test with Mann-Whitney U test)

3. 3. Effect of MAR according to metal direction

The average artifact area before the application of the MAR algorithm was 357.82mm² (SD: 45.78mm²) in the horizontal direction to decrease 131.45mm² (SD: 50.26mm²) after application and decreased from 276.96mm² (SD: 44.53 mm²) to 53.36mm² (SD: 23.09mm²) in the vertical direction. When comparing the decrease in the percentage, it decreased by 63.3% in the horizontal direction and 80.7% in the vertical direction, confirming the effectiveness of the MAR algorithm. The data showed a statistically significant difference in the mean between horizontal and vertical group with a *p*-value of <0.05 when tested by the Mann-Whitney U test for comparison test. (Figure 7) To compare the data, the percentage reduction of parameters was calculated for the vertical group (240 samples: MAR off 120, MAR on 120) and the horizontal group (240 samples: MAR off 120, MAR on 120) to obtain the data. (Table 6)

Table 6. Measured artifact area, differences, and percentage reduction across material direction

Metal direction	MAR Off (mm^2)	MAR on (mm^2)	Difference (mm^2)	Percentage reduction	*p*-value [a]
Horizontal	357.82 ± 45.78	131.45 ± 50.26	267.37 ± 97.19	63.3	<0.05
Vertical	276.96 ± 44.53	53.36 ± 23.09	223.61 ± 24.62	80.7	<0.05

[a] Wilcoxon signed-rank test for compare MAR On and MAR off in the Groups. *p*-value < 0.05 is considered as statistically significant.

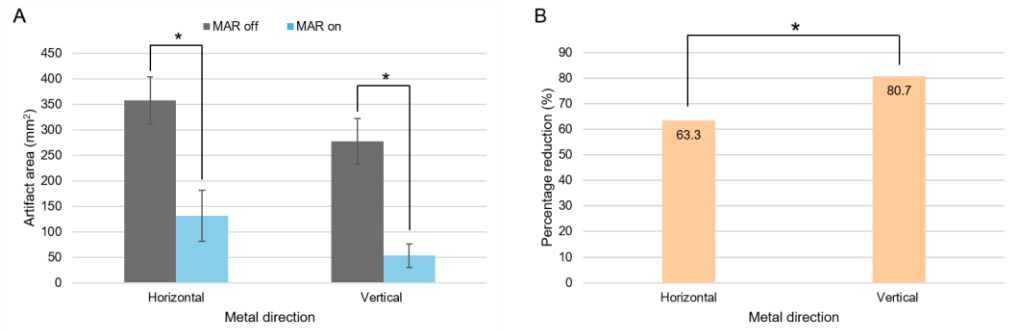

Figure 7. Comparison of metal artifact reduction according to metal direction (A) Measured artifact areas (mm^2) based on metal direction with the MAR algorithm activated and deactivated. Error bars represent standard deviations. (*p <0.05, Wilcoxon signed-rank test). (B) Percentage reduction in artifact areas based on metal direction with the MAR algorithm activated. (*p <0.05, Mann-Whitney U test)

4. DISCUSSION

In this study, we quantitatively evaluated the effectiveness of the MAR algorithm in CBCT using a standardized quality assurance sedentex-CT phantom. The study results showed that metal artifacts were reduced by approximately 70% overall, and it was confirmed that the MAR algorithm effectively reduced artifacts across various exposure protocols and consecutive metal direction, demonstrating the efficacy of the MAR algorithm.

This reduction in artifacts enhances image quality at the same radiation dose, providing visual improvement around areas adjacent to prosthetics. Therefore, it is expected that anatomical structures can be observed more clearly in clinical imaging, contributing to accurate diagnosis and effective treatment planning.

In particular, the MAR algorithm demonstrated a MAR effect regardless of radiation dose, with the ultra-low dose mode notably showing the highest reduction rate at 80.3%. This finding suggests that clinicians may have greater flexibility in choosing imaging settings, especially for patients where radiation exposure is a concern, such as children or pregnant women. Additionally, a low-exposure protocol can be beneficial for patients needing follow-up examinations to monitor their condition periodically (European Society of Cardiology, 2023; De Felice et al., 2019).

In metal direction, vertical direction showed a higher MAR effect, but due to the limitation of FOV of the equipment used in the experiment, the horizontal direction is relatively close to the edge, which can cause a difference in MAR effect. In addition, the results may differ due to the difference in the distance through PMMA from the location (The direction in which the metal rods overlap) where the metal artifacts are most likely to occur when x-rays are transmitted. Although there may be differences depending on the location of the Metal, it is thought that there will be a reduction effect.

Technologies for dental digital equipment, such as intraoral scanners and 3D (Three dimension) printers, have rapidly advanced, and many dental clinics are now utilizing these devices. In particular, to perform implant surgery using a surgical guide, precise CT data for planning implant placement depth and angle, along with scan data for intra-oral placement, are essential. In this process, accurately aligning these two sets of differently acquired data is crucial. For precise alignment, it is important to minimize metal artifacts in the CT data to accurately capture reference points like teeth (Hama & Mahmood, 2023; Wang, Liu, & Deng, 2020; Shi et al., 2023; Apostolakis & Michelinakis, 2020).

In the past, low computer performance caused significant delays in reconstructing scanned images. However, computers equipped with GPU (graphic processing unit) which is recently enable faster processing are available at lower prices. Utilizing GPU performance in image reconstruction can significantly reduce reconstruction time. With improved PC (personal computer) performance, it is now possible to process larger amounts of data in a shorter time, accelerating the development of additional image processing technologies, such as MAR. These advancements in computer performance and reduced costs have broadened the adoption of CBCT in general dentistry, no longer limiting its use to large hospitals (Ghani & Karl, 2020; Valente, António, Mora, & Jardim, 2023).

The experimental methods used in this study are highly significant as CBCT with equivalent or FOV can be tested using quantitative standards with a standardized phantom. These standardized methods are expected to serve as valuable frameworks for future comparisons of various MAR algorithm performances. By consistently comparing and evaluating different metal artifact reduction methods and algorithms provided by numerous manufacturers, we can gain a comprehensive overview of MAR technology.

Although these findings have been confirmed, this study also has some limitations. First, this study focused on evaluating artifacts caused about titanium only, a material commonly used in implants and abutments, by employing a standardized phantom. Consequently, the performance of MAR algorithms for other impermeable materials

used in dental treatments, such as zirconia, stainless steel, and gutta-percha, may differ. Furthermore, since this study mainly assessed the effects of metals on artifact formation, we did not explore the imaging benefits using measured and compared values of signal to noise ratio and carrier to noise ratio for each image. For a more comprehensive assessment in the clinical setting, further studies should include comparison of signal to noise ratio with carrier to noise ratio along with morphological resolution analysis with different materials. Finally, this study specifically evaluated the MAR algorithm using a single CBCT device and the results may differ for different CBCT systems. Future studies should replicate this evaluation across multiple CBCT devices to evaluate the generalizability of the effectiveness of the MAR algorithm.

5. CONCLUSION

This study demonstrates the reduction effectiveness of metal artifacts when applying the MAR function according to radiation dose and metal direction and, in particular, the effect of percentage reduction was excellent when the exposure protocol with low radiation dose and the metal condition were vertical in the scanned CBCT. Therefore, we proposes the standardized experimental methods for quantitative evaluation of metal artifacts in CBCT.

REFERENCES

Zhang, Y., Zhang, L., Zhu, X.R., Dong, L. Lee, A.K., & Chambers, M. (2007). Reducing metal artifacts in cone-beam CT images by preprocessing projection data. International Journal of Radiation Oncology, Biology, Physics, 67(3), 924–932.

Jacobs, R., Salmon, B., Codari, M., Hassan, B., & Bornstein, M. M. (2018). Cone beam computed tomography in implant dentistry: Recommendations for clinical use. BMC Oral Health, 18(88)

Lim, C. H., Jung, H. R., & Lee, M. G. (2005). Management of patient dose in CT examinations (ICRP Publication 87). Computed Tomographic Technology, 1(1), 527.

Korpics, M., Surucu, M., Mescioglu, I., Alite, F., Block, A. M., Choi, M., Emami, B., Harkenrider, M. M., & Solanki, A. (2016). Observer evaluation of a metal artifact reduction algorithm applied to head and neck cone beam computed tomographic images. International Journal of Radiation Oncology, Biology, Physics, 96(4), 897–904.

Queiroz, P. M., Groppo, F. C., Oliveira, M. L., Haiter-Neto, F., & Freitas, D. Q. (2017). Evaluation of the efficacy of a metal artifact reduction algorithm in different cone beam computed tomography scanning parameters. Oral Surgery, Oral Medicine, Oral Pathology, and Oral Radiology, 123(6), 729–734.

Choi, Y. S., Kim, G. T., & Hwang, E. H. (2006). Basic principles of cone beam computed tomography. Korean Journal of Oral and Maxillofacial Radiology, 36, 123–129.

Park, H. S., Jeon, K., & Seo, J. K. (2023). Neural representation-based method for metal-induced artifact reduction in dental CBCT imaging. arXiv.

Barrett, J. F., & Keat, N. (2004). Artifacts in CT: Recognition and avoidance. RadioGraphics, 24(6), 1679–1691.

Washio, H., Ohira, S., Funama, Y., Morimoto, M., Wada, K., Yagi, M., Shimamoto, H., Koike, Y., Ueda, Y., Karino, T., Inui, S., Nitta, Y., Miyazaki, M., & Teshima, T. (2020). Metal artifact reduction using an iterative CBCT reconstruction algorithm for head and neck radiation therapy: A phantom and clinical study. European Journal of Radiology, 132, 109293.

Kunz, A. S., Patzer, T. S., Grunz, J.-P., Luetkens, K. S., Hartung, V., Hendel, R., Fieber, T., Genest, F., Ergün, S., Bley, T. A., & Huflage, H. (2022). Metal artifact reduction in ultra-high-resolution cone-beam CT imaging with a twin robotic X-ray system. Scientific Reports, 12(1), 1-11.

Queiroz, P. M., Oliveira, M. L., Groppo, F. C., Haiter-Neto, F., & Freitas, D. Q. (2017). Evaluation of metal artefact reduction in cone-beam computed tomography images of different dental materials. Clinical Oral Investigations, Online First, 1-5.

Nazir, S. Z., & Mushtaq, M. (2024). Metal artifact reduction by using MARS system of a CBCT unit with different components of fixed orthodontic appliances: An in vitro CBCT analysis. The Journal of Indian Orthodontic Society, 58(3), 252-259.

Kalender, W. A., Hebel, R., & Ebersberger, J. (1987). Reduction of CT artifacts caused by metallic implants. Radiology, 164(2), 576–577.

Yu, L., Li, H., Mueller, J., Kofler, J. M., Liu, X., Primak, A. N., Fletcher, J. G., Guimaraes, L. S., Macedo, T., & McCollough, C. H. (2009). Metal artifact reduction from reformatted projections for hip prostheses in multislice helical computed tomography: Techniques and initial clinical results. Investigative Radiology, 44(11), 691–696.

Boudabbous, S., Arditi, D., Paulin, E., Syrogiannopoulou, A., Becker, C., & Montet, X. (2015). Model-based iterative reconstruction (MBIR) for the reduction of metal artifacts on CT. AJR American Journal of Roentgenology, 205(2), 380–385.

Wang, G., Vannier, M. W., & Cheng, P. C. (1999). Iterative X-ray cone-beam tomography for metal artifact reduction and local region reconstruction. Microscopy and Microanalysis, 5(1), 58–65.

Ghani, M. U., & Karl, W. C. (2020). Fast enhanced CT metal artifact reduction using data domain deep learning. IEEE Transactions on Computational Imaging, 6(1), 181-193.

Lee, H., Kim, S., & Cho, M. K. (2024). Deep learning-based metal extraction with no reference in dental CBCT for metal artifact reduction. In Progress in Biomedical Optics and Imaging - Proceedings of SPIE, Medical Imaging 2024: Image Processing (Vol. 12926). SPIE.

European Society of Cardiology. (2023). European pacing, arrhythmias, and cardiac electrophysiology: Journal of the working groups on cardiac pacing, arrhythmias, and cardiac cellular electrophysiology of the European Society of Cardiology (Europace), 25(2), 270–276.

De Felice, F., Di Carlo, G., Saccucci, M., Tombolini, V., & Polimeni, A. (2019). Dental cone beam computed tomography in children: Clinical effectiveness and cancer risk due to radiation exposure. Oncology, 96(4), 173-178.

Hama, D. R., & Mahmood, B. J. (2023). Comparison of accuracy between free-hand and surgical guide implant placement among experienced and non-experienced dental implant practitioners: An in vitro study. Journal of Periodontal & Implant Science, 53(5), 388-401.

Wang, X., Liu, A., & Deng, W. (2020). Research advances in the use of digital surgical guides in implantology. Hua Xi Kou Qiang Yi Xue Za Zhi / West China Journal of Stomatology, 38(1), 95-100.

Shi, Y., Wang, J., Ma, C., Shen, J., Dong, X., & Lin, D. (2023). A systematic review of the accuracy of digital surgical guides for dental implantation. International Journal of Implant Dentistry, 9(1).

Apostolakis, D., & Michelinakis, G. (2020). Use of CBCT and low-cost additive manufacturing in implant surgical guide fabrication. Compendium of Continuing Education in Dentistry, 41(10), 514-519.

Valente, J., António, J., Mora, C., & Jardim, S. (2023). Developments in image processing using deep learning and reinforcement learning. Journal of Imaging, 9(10), 207.

ABSTRACT IN KOREAN

콘빔 시티의 금속 아티팩트 감소 기능에 대한 정량적 평가: 방사선량과 금속 방향에 따른 평가

목적

최근 콘빔CT를 위한 다양한 금속 아티팩트 감소 (MAR) 기법이 도입되었지만, 그 효과를 정량적으로 평가하는 방법에 대한 근거나 실험 방법이 부족하다. 본 연구는 정도 관리 팬텀을 사용하여 표준화된 실험 방법을 확립하고 촬영된 콘빔CT 이미지에 대한 아티팩트의 면적 측정값을 금속 아티팩트 감소 기능의 사용 전과 후를 비교하여 효과를 평가하는 것을 목표로 한다.

방법

수평 및 수직 방향으로 3개의 원통형 티타늄 막대가 삽입된 sedentex-CT 정도 관리 팬텀을 콘빔CT 장비로 스캔 하였다. 콘빔CT 스캔은 금속 아티팩트 감소 기능 사용 전과 후를 세 가지의 노출 조건(standard, low does, ultra-low does)에서 각각 8회 반복 촬영 및 재구성하여 480 단면을 평가하였다. 모든 이미지의 금속 아티팩트 면적은 ImageJ 소프트웨어를 사용하여 측정하였으며, 각 노출 조건과 금속 막대 방향에 따른 금속 아티팩트 감소 기능의 사용 전과 후의 아티팩트 면적 값 및 감소율의 차이를 통계적으로 분석했다.

결과

금속 아티팩트 감소 기능을 사용한 콘빔CT 이미지의 아티팩트 면적은 모든 노출 모드와 금속 막대 방향에서 금속 아티팩트 감소 기능을 사용하지 않은 면적에 비해 크게 감소하였다. ($p<0.05$). 아티팩트 영역은 ultra-low does (80.3%, 262.30mm²에서 51.72mm²) 에서 가장 큰 감소를 보였고 low dose (73.6%, 331.59mm²에서 87.66mm²)와 standard(61.5%, 358.28mm²에서 137.83mm²)

순서대로 감소 효과를 보였다. 수직 막대 방향(80.7%, 276.96mm²에서 53.36mm²)이 수평 방향(63.3%, 357.82mm²에서 131.45mm²) 보다 효과가 높았다.

결론

본 연구는 다양한 방사선량 조건과 금속 방향에 따른 금속 아티팩트를 감소시키는 알고리즘의 성능을 정량적으로 입증한다. 특히, 촬영된 콘빔CT에서는 방사선량이 적은 노출 프로토콜과 수직 막대방향에서 감소율의 효과가 우수했다. 아티팩트 영역의 정량적인 측정을 포함하는 해당 방법은 향후 임상 분야에서 아티팩트 감소 및 최적화 연구를 위한 귀중한 틀을 제공할 것이다.

핵심되는 말 : 콘빔CT, 금속 아티팩트 감소, 정도관리 팬텀, 촬영 조건, 금속 막대 방향, 감소율